Green's function for magnetostatic surface waves and its application to the study of diffraction patterns

S. Tamaru,[*] J. A. Bain, M. H. Kryder, and D. S. Ricketts[†]

Electrical and Computer Engineering Department, Carnegie Mellon University, Pittsburgh, Pennsylvania 15213, USA

(Received 10 April 2011; published 29 August 2011)

This paper presents the two-dimensional (2D) Green's function (GF) of magnetostatic surface waves (MSSWs) in real space and the frequency domain, i.e., the spatial propagation pattern of MSSWs emitted by a point wave source in a tangentially magnetized slab geometry, including the effect of finite damping. The theory first derives an inhomogeneous differential equation of the spin system under a magnetostatic approximation. This equation is translated into a Sturm-Liouville problem by introducing a Hermitian operator, and solved by the eigenfunction expansion technique, which yields an integral expression of the GF in the form of a 2D inverse Fourier transform. The obtained GF demonstrates various features characteristic of MSSWs, such as strongly anisotropic propagation, angular confinement of energy flow from the wave source whose limit angle is defined as the critical angle for the group velocity θ_g, and semicaustic beams along θ_g. We then calculate the 1D spatial profiles and 2D diffraction patterns of MSSW propagation by convolving the GF with various wave source distributions, and compare them with experimental results observed on a tangentially magnetized Permalloy film. Comparison between these numerical and experimental results shows excellent agreement.

DOI: 10.1103/PhysRevB.84.064437 PACS number(s): 75.30.Ds, 75.40.Gb, 75.50.Bb, 76.50.+g

I. INTRODUCTION

Magnetostatic waves (MSWs) have been a subject of intensive research for more than five decades as a fundamental excitation mode in high-frequency magnetization dynamics. If a film is tangentially magnetized, rotational symmetry about the axis normal to the film is broken. This results in anisotropic wave propagation of MSWs. Such behaviors have been both theoretically derived[1,2] and experimentally observed[3,4] by many researchers.

Until the last decade, the most widely used experimental techniques for the study of MSWs were (1) inductive probing, which picks up ac magnetic fields using a coil[4,5] and (2) Brillouin light scattering (BLS), which detects inelastic scattering of a plane optical wave by a plane MSW.[6,7] Since neither of these can capture dynamic magnetization with a high lateral resolution, most theoretical studies about the response of the dynamic magnetization to excitation fields assumed either an excitation field distribution having the form of a plane wave or a laterally 1D system,[8–11] in order to be applicable to these techniques.

While these studies are quite useful for analyzing wide MSW beams, many source distributions have a finite, nonuniform spatial geometry that emits laterally confined MSWs. Such situations have been attracting increased interest with the recent introduction of two experimental techniques, microfocus BLS (MF-BLS)[12–19] and spatially resolved ferromagnetic resonance scanning Kerr effect microscopy (SRFMR-SKEM),[20–23] which can measure both amplitude and phase of local dynamic magnetization with sub-μm lateral resolution.[16,21] These techniques opened doors for studying various wave physics problems of MSWs such as diffraction, interference, spatial eigenmode profiles, scattering, and so on. In order to analyze the results obtained by these new techniques and understand the underlying wave physics in spin systems, another form of response function is strongly sought, namely the Green's function (GF) in real space and the frequency domain for a laterally 2D system, $\vec{m}(\vec{r},\omega)$.

Physically, the GF represents the spatial distribution of fields emitted by a point field source. Mathematically, it is an integral kernel of inhomogeneous linear differential equations appearing in various field problems. Once this information is provided, many problems can be solved simply by convolving it with the field source distribution. The GF is such a fundamental piece of knowledge that it has been derived for many standard differential equations such as Poisson's equation, Helmholtz's equation, diffusion equation to name a few. But the systems for which the GF has been derived typically have a high degree of symmetry that greatly simplifies its mathematical derivation. On the other hand, a tangentially magnetized slab geometry requires very complicated mathematical treatment due to its low symmetry. There have been some past studies that attempted to derive the GF of MSWs.[10,19,24–26] To the author's knowledge, however, they were either incomplete or significantly simplified to circumvent such complexity, and therefore their applicability is limited.

The goal of this work is to present the two-dimensional (2D) GF of magnetostatic surface waves (MSSWs) excited in a tangentially magnetized slab geometry including the effect of finite damping. This paper consists of two main parts. The first part is the calculation of the GF of MSSWs. In this part, the mathematical theory for deriving the expression of the GF is first described, then an algorithm for performing the numerical calculation of it is presented, and finally various features of the GF obtained by our approach are discussed. The theory starts with the combination of the Landau-Lifshitz equation and Maxwell's equations in the magnetostatic limit, which leads to an inhomogeneous differential equation of the spin system having two source terms of different physical origins. This is translated into a Sturm-Liouville problem by introducing a Hermitian operator, and solved by the standard eigenfunction expansion technique, which yields an integral expression of the two GFs in the form of the 2D inverse Fourier transform. We also introduce a finite Gilbert damping in the theory and calculate the GFs for a lossy system. The GFs

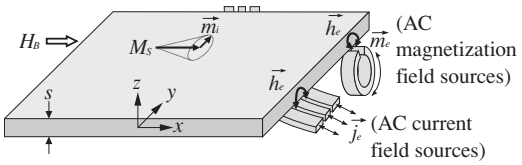

FIG. 1. Arrangement of the magnetic film, static/dynamic magnetization, dc bias field and ac excitation field sources modeled in this work, along with the coordinate definition.

of MSSWs obtained by this approach show various features characteristic of MSSWs, such as an anisotropic propagation pattern, angular confinement of energy flow from the point wave source, whose limit angle is defined as the critical angle for the group velocity θ_g, and semicaustic beams along θ_g. The second part presents the application of the GF of MSSWs to the reconstruction of spatial MSSW propagation patterns, and the comparison between the numerically calculated and experimentally measured spatial patterns. Three cases are presented in this work: one for 1D propagation along the direction perpendicular to the bias field, and two for 2D diffraction patterns around different irregularities. The measurements are done on a tangentially magnetized Permalloy (Py) film using SRFMR-SKEM. The numerical calculation corresponding to each measurement is performed by convolving the GF of MSSWs with the wave source distribution calculated from the sample geometry. These results are compared to examine the validity of the GFs of MSSWs obtained in this work.

II. CALCULATION OF THE GREEN'S FUNCTION OF MSSWs

A. Definition of the problem

Figure 1 shows the arrangement of the system to be modeled. We will consider how MSSWs are excited by an arbitrary distribution of ac excitation fields $\vec{h}_e$, and how they propagate in an infinitely large magnetic film with a saturation magnetization M_S and a thickness s, tangentially magnetized by an external dc bias field H_B, applied along the x axis. The film is assumed to be lossless in the beginning of the mathematical derivation, and a finite Gilbert damping α is introduced later. The dynamic magnetization in the film due to MSSW excitation and the dynamic field associated with it are denoted as $\vec{m}_i$ and $\vec{h}_i$, respectively. Excitation field sources, such as ac current density $\vec{j}_e$ and ac magnetization distribution $\vec{m}_e$, exist only in the exterior of the magnetic film. The film thickness s is much smaller than distances between the magnetic film and these excitation field sources such that $\vec{h}_e$ in the interior of the film can be approximated as uniform across the film thickness, and also much smaller than the skin depth of electromagnetic fields such that eddy currents are negligible. In the following discussion, we assume that the dynamic quantities are much smaller than the static ones, i.e., $m_i \ll M_S$ and $h_i, h_e \ll H_B$. Exchange fields and anisotropy fields are ignored, meaning that the excitation mode considered here is pure MSSWs propagating in an isotropic soft magnetic film. The coordinate origin is set at the middle of the film thickness. The SI unit system is followed throughout this work.

Some other notations are given here for clarity.

(i) $\vec{r} = (x,y,z)$: position vector in real space;

(ii) $\vec{r}_t = (x,y)$: transverse position vector in real space; if it is operated with $\vec{r}$, $\vec{r}_t = (x,y,0)$;

(iii) $\vec{k} = (k_x,k_y,k_z)$: wave vector (position vector in inverse space);

(iv) $\vec{k}_t = (k_x,k_y)$: transverse wave vector (transverse position vector in inverse space); if it is operated with $\vec{k}$, $\vec{k}_t = (k_x,k_y,0)$;

(v) $\vec{e}_x,\vec{e}_y,\vec{e}_z$: unit vector along the axis specified by the index;

(vi) a decay constant q_z may be used to replace k_z such that $iq_z = k_z$;

(vii) the superscript i or e of variables signifies that the variable is either for the interior or exterior of the film, e.g., q_z^i is the decay constant along the z axis for the interior of the film;

(viii) t is time, f is frequency, and $\omega = 2\pi f$ is angular frequency;

(ix) the integration range is $\pm\infty$ unless specified otherwise;

(x) The Fourier transform (FT) and inverse Fourier transform (iFT) used in this work are defined as

$$\mathcal{F}_{\vec{r}}[f] = \frac{1}{(2\pi)^{n/2}} \int f(\vec{r}) e^{-i\vec{k}\cdot\vec{r}} d^n r, \tag{1}$$

$$\mathcal{F}^{-1}_{\vec{k}}[g] = \frac{1}{(2\pi)^{n/2}} \int g(\vec{k}) e^{i\vec{k}\cdot\vec{r}} d^n k, \tag{2}$$

where the subscript is the variable vector along which the transform is performed and n is its dimension

(xi) a Gaussian distribution with the standard deviation of σ in real and inverse space is denoted as

$$\phi^r_\sigma(\vec{r}) = \mathcal{F}^{-1}_{\vec{k}}\left[\phi^i_\sigma\right] = \frac{1}{(2\pi)^{n/2}\sigma^n} \exp\left(-\frac{|\vec{r}|^2}{2\sigma^2}\right), \tag{3}$$

$$\phi^i_\sigma(\vec{k}) = \mathcal{F}_{\vec{r}}\left[\phi^r_\sigma\right] = \frac{1}{(2\pi)^{n/2}} \exp\left(-\frac{\sigma^2|\vec{k}|^2}{2}\right), \tag{4}$$

where n is the dimension of the variable vector.

B. Inhomogeneous differential equation for MSWs excited in a tangentially magnetized slab geometry

The first step of this modeling is to derive the inhomogeneous differential equation for MSWs. According to the Damon-Eshbach (DE) theory, either magnetostatic backward volume waves (MSBVW) or MSSWs are excited in a tangentially magnetized slab geometry depending on the condition.[1] We will first construct a theory applicable to both modes, then limit our discussion to MSSWs when necessary.

We begin with the Landau-Lifshitz (LL) equation, which describes the dynamics of a single magnetic moment without damping:[27]

$$\frac{d\vec{M}}{dt} = -\gamma \vec{M} \times \vec{H}, \tag{5}$$

where $\vec{M}$ is the magnetization, $\vec{H}$ is the magnetic field, $\gamma = \mu_0 g q_e / 2m_e$ is the gyromagnetic constant, μ_0 is the vacuum permeability, g is Lande g factor, q_e is the electron charge, and m_e is the electron mass.

The condition that the dynamic terms are much smaller than the static terms allows one to decompose the magnetic field and the magnetization into a static and a dynamic part as

$$\vec{H} = H_B\vec{e}_x + \vec{h}e^{-iwt}, \tag{6}$$
$$\vec{M} = M_S\vec{e}_x + \vec{m}e^{-iwt}, \tag{7}$$

where $\vec{h}$ and $\vec{m}$ are the amplitude vectors of the dynamic part of the field and the magnetization, respectively. By plugging Eqs. (6) and (7) into Eq. (5), dropping the second-order terms, and solving the equation in terms of $\vec{m}$, the linearized equation of motion for a magnetic moment is obtained:

$$\vec{m} = P\vec{h}, \tag{8}$$

where

$$P = \begin{pmatrix} 0 & 0 & 0 \\ 0 & \chi & -i\kappa \\ 0 & i\kappa & \chi \end{pmatrix},$$
$$\chi = \frac{\omega_H\omega_M}{\omega_H^2 - \omega^2},$$
$$\kappa = \frac{\omega\omega_M}{\omega_H^2 - \omega^2},$$

$\omega_H = \gamma H_B$ and $\omega_M = \gamma M_S$. The coefficient matrix P is the dynamic susceptibility tensor (Polder tensor), which represents the linear relationship between the ac field and the dynamic response of the magnetization.

In this work, we focus on the behavior of spin waves under a magnetostatic approximation. The physical meaning of this is that the wavelength of the spin wave, λ, is much shorter than the distance over which electromagnetic fields propagate within one cycle, i.e., $c \gg f\lambda$, where c is the speed of light. This condition allows the displacement current to be ignored. Also, eddy currents are negligible, as mentioned above. In this case, Maxwell's equations for magnetic fields are completely separated from those for electric fields. By plugging Eqs. (6) and (7) into Maxwell's equations for magnetic fields, Gauss' law and Ampere's law for the dynamic terms are obtained:

$$\nabla\cdot(\vec{h} + \vec{m}) = 0, \tag{9}$$
$$\nabla\times\vec{h} = \vec{j}_e. \tag{10}$$

By definition, the total dynamic magnetic field is the sum of the dynamic fields due to MSW excitation and the ac excitation fields,

$$\vec{h} = \vec{h}_i + \vec{h}_e. \tag{11}$$

$\vec{h}_e$ can be expressed by $\vec{j}_e$ and $\vec{m}_e$ as

$$4\pi\vec{h}_e(\vec{r}) = \nabla\times\int\frac{\vec{j}_e(\vec{r}')}{|\vec{r}-\vec{r}'|}d^3r' + \nabla\int\frac{\nabla'\cdot\vec{m}_e(\vec{r}')}{|\vec{r}-\vec{r}'|}d^3r'. \tag{12}$$

It is clear that these quantities satisfy

$$\nabla\cdot\vec{h}_e = -\nabla\cdot\vec{m}_e, \tag{13}$$
$$\nabla\times\vec{h}_e = \vec{j}_e. \tag{14}$$

A function $u(z)$ that signifies the interior of the magnetic film is introduced as

$$u(z) = \begin{cases} 0 & |z| > s/2, \\ 1/2 & |z| = s/2, \\ 1 & |z| < s/2. \end{cases} \tag{15}$$

The derivative of u is

$$\frac{du}{dz} = \delta(z + s/2) - \delta(z - s/2), \tag{16}$$

where $\delta(z)$ is Dirac's delta function. The total dynamic magnetization can be expressed by using Eqs. (8), (11), and (15) as

$$\vec{m} = \vec{m}_i + \vec{m}_e = uP(\vec{h}_i + \vec{h}_e) + \vec{m}_e. \tag{17}$$

By using Eqs. (11) and (17), Gauss's law, Eq. (9), and Ampere's law, Eq. (10), can be written as

$$\nabla\cdot\{\vec{h}_i + \vec{h}_e + uP(\vec{h}_i + \vec{h}_e) + \vec{m}_e\} = 0, \tag{18}$$
$$\nabla\times(\vec{h}_i + \vec{h}_e) = \vec{j}_e. \tag{19}$$

Sources of the ac excitation fields are assumed to exist only in the exterior of the film. Therefore the following equations hold:

$$u\nabla\cdot\vec{h}_e = -u\nabla\cdot\vec{m}_e = 0, \tag{20}$$
$$u\nabla\times\vec{h}_e = u\vec{j}_e = 0. \tag{21}$$

Equation (18) can be expanded by using Eqs. (8), (13), (16), (20), and (21) as

$$\nabla\cdot(\vec{h}_i + uP\vec{h}_i) = \chi u\frac{\partial h_{ex}}{\partial x} - \frac{du}{dz}P\vec{h}_e\cdot\vec{e}_z. \tag{22}$$

The physical meaning of each of the two terms in the right-hand side (RHS) is as follows. The first term is due to "fictitious" volume charges. When a magnetic flux enters the magnetic film from the y-z plane, it acts on a magnetic moment to tip it away from the x axis. If the flux changes its direction from within the y-z plane to the x axis, it becomes parallel to the magnetization and therefore exerts no torque on the magnetic moment. This is equivalent to the disappearance of the magnetic flux in the film. This situation looks as if a magnetic volume charge exists in the film which absorbs the flux line. The second term is due to surface charges induced at the boundaries as a result of tipping of the magnetization by the application of ac excitation fields.

Now let us turn to Ampere's law for the dynamic terms, Eq. (19). This can be written by using Eq. (14) as

$$\nabla\times\vec{h}_i = 0. \tag{23}$$

This permits the introduction of a magnetic scalar potential ψ such that

$$h_i = -\nabla\psi, \tag{24}$$

as in the DE theory. By using ψ, Eq. (22) becomes

$$-\nabla\cdot(\nabla + uP\nabla)\psi = \chi u\frac{\partial h_{\rm ex}}{\partial x} - \frac{du}{dz}P\vec{h}_e\cdot\vec{e}_z. \tag{25}$$

This is the inhomogeneous differential equation ψ must satisfy under an arbitrary distribution of ac excitation fields. As stated in the definition of the problem, the film is thin enough that $\vec{h}_e$ can be approximated as uniform across the film thickness.

This reduces the problem to two dimensions and the magnetic potential can be expressed by introducing the following two kinds of GFs. One is the GF for fictitious volume charges G_V, defined by

$$-\nabla\cdot(\nabla+uP\nabla)G_V=u\delta(x)\delta(y). \tag{26}$$

The other is the GF for surface charges G_S, defined by

$$-\nabla\cdot(\nabla+uP\nabla)G_S=-\frac{du}{dz}\delta(x)\delta(y). \tag{27}$$

Once these two GFs are obtained, the magnetic potential due to MSW excitation for any field source distribution can be obtained by first calculating $\vec{h}_e$ using Eq. (12) and next performing the following convolution integral:

$$\psi(\vec{r})=\int\left[G_V(\vec{r}-\vec{r}_t')\chi\frac{\partial h_{\rm ex}}{\partial x'}+G_S(\vec{r}-\vec{r}_t')P\vec{h}_e(\vec{r}_t')\cdot\vec{e}_z\right]d^2r_t'. \tag{28}$$

C. Introduction of the MSW operator

The differential equations for the two kinds of GFs, Eqs. (26) and (27), have a nonstandard, complicated form. In order to solve these equations, we introduce a MSW operator $\mathfrak{M}$, which represents the whole operator appearing in the left-hand side (LHS) of these equations:

$$\mathfrak{M}=-\nabla\cdot(\nabla+uP\nabla). \tag{29}$$

This operator can be expanded as

$$\mathfrak{M}=-\nabla^2-\chi u\left(\frac{\partial^2}{\partial y^2}+\frac{\partial^2}{\partial z^2}\right)-\frac{du}{dz}\left(i\kappa\frac{\partial}{\partial y}+\chi\frac{\partial}{\partial z}\right). \tag{30}$$

It can be easily understood that $\mathfrak{M}$ takes the following forms in the exterior and interior of the film, respectively,

$$\mathfrak{M}=\begin{cases}-\left(\frac{\partial^2}{\partial x^2}+\frac{\partial^2}{\partial y^2}+\frac{\partial^2}{\partial z^2}\right) & |z|>s/2,\\ -\frac{\partial^2}{\partial x^2}-(1+\chi)\left(\frac{\partial^2}{\partial y^2}+\frac{\partial^2}{\partial z^2}\right) & |z|<s/2.\end{cases} \tag{31}$$

Thus the equation $\mathfrak{M}\psi=0$ becomes the standard Laplace's or Walker's equation depending on the range of z except at the boundaries.

In order to obtain the form of $\mathfrak{M}$ at the boundaries, the treatment of a discontinuity must be clearly defined. ψ has to be continuous over the boundaries. However, its derivative has discontinuities because it generally has a sharp cusp at the boundary. The first partial derivative with respect to z at the boundary is defined as the average of the derivatives calculated as the limit value from the negative and positive side,

$$\left.\frac{\partial}{\partial z}\right|_{z=\pm s/2}=\frac{1}{2}\left(\left.\frac{\partial}{\partial z}\right|_{z\to\pm s/2+0}+\left.\frac{\partial}{\partial z}\right|_{z\to\pm s/2-0}\right), \tag{32}$$

where $z\to s/2+0$ signifies that z approaches to $s/2$ from the positive side, and vice versa. The second partial derivative is defined as having a delta function at the boundary whose magnitude is the height of the discontinuity in the first derivative,

$$\left.\frac{\partial^2}{\partial z^2}\right|_{z=\pm s/2}=\delta(z\mp s/2)\left(\left.\frac{\partial}{\partial z}\right|_{z\to\pm s/2+0}-\left.\frac{\partial}{\partial z}\right|_{z\to\pm s/2-0}\right). \tag{33}$$

By substituting these equations into Eq. (30), it can be shown that $\mathfrak{M}$ takes the following form at the boundaries:

$$\begin{aligned}\mathfrak{M}|_{z=\pm s/2}=&-\left.\frac{\partial^2}{\partial x^2}\right|_{z=\pm s/2}-(1+\chi/2)\left.\frac{\partial^2}{\partial y^2}\right|_{z=\pm s/2}\\ &\pm\delta(z\mp s/2)\left\{i\kappa\left.\frac{\partial}{\partial y}\right|_{z=\pm s/2}+(1+\chi)\left.\frac{\partial}{\partial z}\right|_{z\to\pm s/2\mp0}\right.\\ &\left.-\left.\frac{\partial}{\partial z}\right|_{z\to\pm s/2\pm0}\right\}.\end{aligned} \tag{34}$$

In this equation, the coefficient term of the delta function must be zero in order for $\mathfrak{M}\psi$ to be finite at the boundaries. This requirement yields the following equation:

$$i\kappa\left.\frac{\partial}{\partial y}\right|_{z=\pm s/2}+(1+\chi)\left.\frac{\partial}{\partial z}\right|_{z\to\pm s/2\mp0}=\left.\frac{\partial}{\partial z}\right|_{z\to\pm s/2\pm0}. \tag{35}$$

This is, when acting on ψ, exactly the same as the standard magnetic boundary condition that normal component of the magnetic induction is continuous, i.e.,

$$(h_{iz}+m_{iz})|_{\rm interior}=h_{iz}|_{\rm exterior}. \tag{36}$$

In addition, the requirement that the potential function is continuous over the boundaries is equivalent to the other boundary condition that the tangential component of the magnetic field is continuous. From the above discussion, it has been shown that the MSW operator $\mathfrak{M}$ contains all the conditions the potential function ψ must satisfy. Therefore the differential equation

$$\mathfrak{M}\psi=0 \tag{37}$$

gives the very MSW solution as derived in the DE theory.

D. Eigenfunctions of the MSW operator

In this subsection, it is first shown that $\mathfrak{M}$ is Hermitian. Then the eigenfunctions of this operator are derived and their properties are examined for the purpose of expanding the GF with them. The discussion up to this point has not been limited to the mode of magnetic excitation, meaning that the formalism presented so far is applicable to both MSBVWs and MSSWs. From this subsection on, we limit our discussion to only MSSWs. Mathematically, this means that $1+\chi>0$ holds in the following. This leads to the fact that there is only one solution that satisfies Eq. (37), since only one dispersion surface exists for MSSWs. This greatly reduces the burden for performing the numerical calculation, as shown later. However, the theory itself presented in the following should be applicable to both MSBVWs and MSSWs. If the GF of MSBVWs is sought, one only needs to extend the following discussion to take into account the multiplicity of the MSBVW solutions.

The eigenfunctions of $\mathfrak{M}$, Γ, are defined as the solution of this equation

$$\mathfrak{M}\Gamma = \varepsilon\Gamma, \tag{38}$$

where ε is the eigenvalue associated with the eigenfunction. It can be easily understood from Eq. (31) that $\mathfrak{M}$ is a separable operator. Thus the eigenfunction should have the following form:

$$\Gamma(x,y,z) = \Gamma_x(x)\Gamma_y(y)\Gamma_z(z). \tag{39}$$

By plugging this and Eq. (31) into Eq. (38), it can be shown that the general form of Γ_x, Γ_y and Γ_z, becomes

$$\Gamma_x(x) = e^{ik_x x}, \tag{40}$$

$$\Gamma_y(y) = e^{ik_y y}, \tag{41}$$

$$\Gamma_z(z) = \begin{cases} C_3 e^{-q_z^e z} + C_4 e^{q_z^e z} & z > s/2, \\ C_1 \cosh\left(q_z^i z\right) + C_2 \sinh\left(q_z^i z\right) & |z| \leqslant s/2, \\ C_5 e^{-q_z^e z} + C_6 e^{q_z^e z} & z < -s/2, \end{cases} \tag{42}$$

where $C_n (n = 1 \ldots 6)$ are constants. It should be noted that both k_x and k_y are always real while q_z^i and q_z^e may be either real or imaginary, but cannot take a general complex value, as we will show later.

It can be shown that $\mathfrak{M}$ is Hermitian. It is obvious that Γ_x and Γ_y, as given in Eqs. (40) and (41), are the function space of the Fourier transform, which satisfies all the Hermitianity conditions. Therefore it is sufficient to show that $\mathfrak{M}$ is Hermitian along the z axis. By substituting Eqs. (40) and (41) into Eq. (30), the MSW operator along the z axis, $\mathfrak{M}_z$, can be written as

$$\mathfrak{M}_z = -\frac{d}{dz}\left\{(1+\chi u)\frac{d}{dz}\right\} + k_x^2 + (1+\chi u)k_y^2 + \kappa\frac{du}{dz}k_y. \tag{43}$$

In general, an operator having a form of

$$\mathcal{L} = -\frac{d}{dz}\left\{p(z)\frac{d}{dz}\right\} + q(z) \tag{44}$$

is called a Sturm-Liouville operator, which is always Hermitian as long as $p(z)$ and $q(z)$ are both real. It is clear that $\mathfrak{M}_z$ is a Sturm-Liouville operator as both χ and κ are real under the lossless condition. Hermitianity of $\mathfrak{M}$ leads to the following three postulates:

(i) the eigenvalues ε are always real;
(ii) the eigenfunctions Γ_z form a complete set;
(iii) the eigenfunctions associated with different eigenvalues are orthogonal.

Now the properties of the eigenfunctions are examined in more detail. Substituting Eqs. (39)–(42) and (31) into Eq. (38) yields the following relations:

$$k_x^2 + k_y^2 - {q_z^e}^2 = \varepsilon, \tag{45}$$

$$k_x^2 + (1+\chi)\left(k_y^2 - {q_z^i}^2\right) = \varepsilon. \tag{46}$$

It can be easily understood from these equations that both q_z^e and q_z^i are either pure real or pure imaginary because k_x, k_y, ε, and $1+\chi$ are all real, and therefore ${q_z^e}^2$ and ${q_z^i}^2$ are also both real, which may be either negative or positive. Equating these equations yields

$${q_z^e}^2 = (1+\chi){q_z^i}^2 - \chi k_y^2. \tag{47}$$

It should be noted first that χ is always negative because the frequency of magnetic excitations is always higher than the Zeeman frequency, i.e., $\omega > \omega_H$, and second that $1+\chi$ is positive for MSSW excitation as stated above. From Eq. (47), it can be understood that there are three types of eigenfunctions:

(1) Both q_z^e and q_z^i are real.
(2) q_z^e is real, q_z^i is imaginary.
(3) Both q_z^e and q_z^i are imaginary.

Properties of eigenfunctions belonging to each of these three cases will be discussed below. In the following, k_y is limited to non-negative because the eigenequation contains only k_y^2, as shown later, so $\pm k_y$ give the same solution. Also, k_z^i or q_z^i, whichever real, and q_z^e are limited to non-negative for cases (1) and (2) without losing generality, because the eigenfunction Γ_z behaves like a guided wave for these cases and the sign of k_z^i or q_z^i makes no difference in the resultant eigenfunction, and the sign of q_z^e must be chosen such that Γ_z converges at $\pm\infty$.

Case (1): Both q_z^e and q_z^i are real. In this case, C_4 and C_5 in Eq. (42) must be zero in order for Γ_z to converge to zero at $z \to \pm\infty$. Therefore Γ_z can be written as

$$\Gamma_z(z) = \begin{cases} C_3 e^{-q_z^e z} & z > s/2, \\ C_1 \cosh\left(q_z^i z\right) + C_2 \sinh\left(q_z^i z\right) & |z| \leqslant s/2, \\ C_6 e^{q_z^e z} & z < -s/2. \end{cases} \tag{48}$$

The eigenequation for this case can be obtained by the same procedure as for deriving the characteristic equation of the MSSW solution in the DE theory. From the continuity requirement at the boundaries, C_3 and C_6 are eliminated. Next, plugging Eq. (48) into Eq. (35) yields simultaneous linear equations of C_1 and C_2. The requirement that C_1 and C_2 take nontrivial values and eliminating q_z^e using Eq. (47) give the following eigenequation:

$$(1+\chi)(2+\chi){q_z^i}^2 - (\kappa^2+\chi){k_y}^2 + 2(1+\chi)q_z^i\sqrt{(1+\chi){q_z^i}^2 - \chi{k_y}^2}\coth\left(q_z^i s\right) = 0. \tag{49}$$

It should be noted that Eq. (49) contains only two variables q_z^i and k_y. This means that q_z^i is a function of only k_y and independent of k_x.

For explanations given below, two values are examined here. The first is the behavior of k_y in the limit of $q_z^i \to 0$. Noting that $\lim_{z\to 0} z\coth z = 1$, it can be shown that k_y approaches either 0 or a constant η, given as

$$\eta s = \frac{2\sqrt{-\chi}(1+\chi)}{\kappa^2+\chi}. \tag{50}$$

The second is the minimum value of k_y that gives $\varepsilon = 0$, which we denote as k_m. This is the wave number of the MSSW propagating along the y axis, i.e., the solution of Eq. (37) with $k_x = 0$, given by the following equation:

$$k_m s = -\frac{1}{2}\ln\left(1 - 4\frac{\omega^2 - \omega_K^2}{\omega_M^2}\right), \tag{51}$$

where ω_K is the Kittel frequency given by

$$\omega_K^2 = \omega_H(\omega_H + \omega_M). \tag{52}$$

The eigenequation, Eq. (49), and its solution have the following properties:

(i) η is always smaller than k_m.

(ii) Equation (49) has one real solution of q_z^i when $k_y \geqslant \eta$. In other words, q_z^i is a real function of k_y in this range. Hereafter, this solution is denoted as q_{z0}^i.

(iii) q_z^i becomes imaginary when $k_y < \eta$ [therefore Eq. (49) does not have a solution belonging to case (1) in this range].

(iv) The point $k_y = \eta$ is a branch point on the Riemann surface of the function $q_{z0}^i(k_y)$.

(v) The eigenfunction Γ_z, as given by substituting $q_z^i = q_{z0}^i(k_y)$ into Eq. (48), is a real function. This property corresponds to the fact that the amplitude of this eigenfunction is confined around the magnetic film and Γ_z behaves like a guided wave.

(vi) Case (1) corresponds to the MSSW solution, which can exist under the condition of $1 + \chi > 0$. Thus only this case can give $\varepsilon = 0$.

Case (2): q_z^e is real and q_z^i is imaginary. In this case too, C_4 and C_5 must be zero for the same reason as in case (1). As for the form of Γ_z, it is more convenient to adopt trigonometric functions since q_z^i is imaginary:

$$\Gamma_z(z) = \begin{cases} C_3 e^{-q_z^e z} & z > s/2, \\ C_1 \cos\left(k_z^i z\right) + C_2 \sin\left(k_z^i z\right) & |z| \leqslant s/2, \\ C_6 e^{q_z^e z} & z < -s/2. \end{cases} \tag{53}$$

The eigenequation for this case can be derived simply by plugging $iq_z^i = k_z^i$ into Eq. (49):

$$(1+\chi)(2+\chi){k_z^i}^2 + (\kappa^2+\chi)k_y^2 - 2(1+\chi)k_z^i\sqrt{-(1+\chi){k_z^i}^2 - \chi k_y^2}\cot\left(k_z^i s\right) = 0. \tag{54}$$

As for case (1), Eq. (54) contains only k_z^i and k_y. Thus k_z^i is a function of only k_y. However, k_z^i may not be uniquely determined for a given k_y due to the multivaluedness of $\cot^{-1}(k_z^i s)$. In fact, a finite number of discrete k_z^i can generally satisfy Eq. (54). These discrete solutions are labeled as k_{zn}^i where n is an integer. Bearing this in mind, the eigenequation, Eq. (54), has the following properties:

(i) Equation (54) has one real solution of k_z^i when $k_y \leqslant \eta$, which is analytically continuous to q_{z0}^i for case (1). Hereafter, this solution is denoted as $k_{z0}^i = iq_{z0}^i$.

(ii) Equation (54) has zero or a finite number of real solutions of k_z^i when $k_y > \eta$, which are denoted as k_{zn}^i.

(iii) k_{zn}^i satisfies $n\pi < k_{zn}^i s < (n + 1/2)\pi$ if it exists.

(iv) When Eq. (54) has real k_{zn}^i solutions, the eigenfunction Γ_z, as given by substituting the k_{zn}^i into Eq. (53), becomes a real function due to the same reason as for case (1).

(v) Case (2) corresponds to the MSBVW solution, which cannot exist under the condition of $1 + \chi > 0$. Thus this case cannot give $\varepsilon = 0$.

Case (3): Both q_z^e and q_z^i are imaginary. In this case, C_4 and C_5 do not have to be zero since q_z^e is imaginary and therefore Γ_z becomes oscillatory. Thus the eigenfunction has six coefficients while the boundary conditions provide only four equations, which are not enough for eliminating all the coefficients and uniquely determining the value of q_z^i for a given $\vec{k}_t$. In other words, $iq_z^i = k_z^i$ and $iq_z^e = k_z^e$ can take continuous values. This corresponds to the fact that the amplitude is not confined around the film but spreads over the entire range of z. This is physically similar to the leaky modes appearing in 2D waveguide problems. Likewise, cases (1) and (2) are similar to the surface and bulk guided modes, respectively. The properties of case (3) are summarized as follows:

(i) k_z^i can take continuous values;

(ii) the eigenfunction Γ_z for case (3) is oscillatory and complex;

(iii) the amplitude of Γ_z for case (3) is not confined around the film, but spreads over the entire range of z;

(iv) no value of q_z^i in case (3) can give $\varepsilon = 0$.

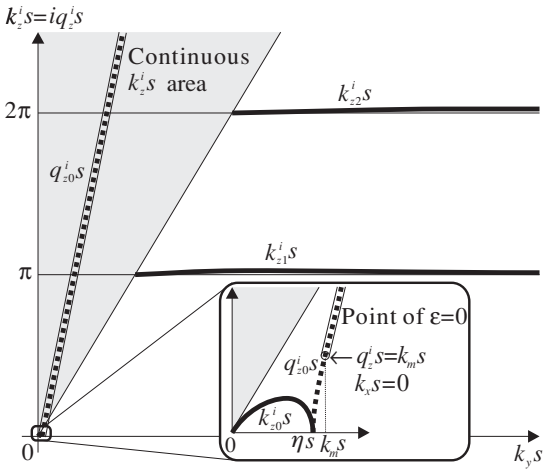

FIG. 2. Behavior of $k_z^i = iq_z^i$ as a function of k_y. Notice that all the quantities shown in this figure are normalized by the film thickness s. The parameters used for this calculation are $H_B = 5.03 \times 10^3$ A/m, $f = 8$ GHz, $M_S = 7.96 \times 10^5$ A/m, and $\gamma = 2.39 \times 10^4$ rad m/s A. The solid and broken lines show k_{zn}^i and q_{z0}^i, respectively. The shaded area shows the region where k_z^i takes continuous values. The point of $\varepsilon = 0$ moves on the real q_{z0}^i line. The minimum value of k_y, which can give $\varepsilon = 0$, occurs when $k_x = 0$ and $k_y = q_z^i = k_m$, given by Eq. (51).

(iv) the point of $\varepsilon = 0$ moves to the larger k_y direction on the q_{z0}^i line, but never goes to any of the k_{zn}^i lines under the condition of $1 + \chi > 0$.

Figure 2 shows the behavior of $k_z^i = iq_z^i$ as a function of k_y along with the movement of the point that can give $\varepsilon = 0$. Notice that all the quantities shown in this figure are normalized by the film thickness s. Only one line for q_{z0}^i exists, while multiple lines for k_{zn}^i exist. In the shaded area, k_z^i takes continuous values. The point of $\varepsilon = 0$ starts at $k_y = k_m$ on the q_{z0}^i line. At this point, $q_{z0}^i = k_m$ and $k_x = 0$ hold. As $|k_x|$ becomes larger, the point of $\varepsilon = 0$ moves to the larger k_y direction on the q_{z0}^i line, but never goes to any of the k_{zn}^i lines under the condition of $1 + \chi > 0$.

E. Expansion of the Green's function with the eigenfunctions of the MSW operator

In order to write the general form of the inhomogeneous differential equations for the two kinds of GFs, the inhomogeneous term is denoted as $F(z)$:

$$F(z) = \begin{cases} F_V(z) = u(z), \\ F_S(z) = \delta(z - s/2) - \delta(z + s/2), \end{cases} \tag{55}$$

where F_V and F_S are for fictitious volume charges and surface charges, respectively. Using this notation, Eqs. (26) and (27) can be written as

$$\mathfrak{M}G = \delta(x)\delta(y)F(z). \tag{56}$$

The GF, which may be either G_V or G_S, can be expanded with the eigenfunctions as

$$G(\vec{r}) = \sum_{k_z^i} \mathcal{F}^{-1}_{\vec{k}_t}\left[\frac{\Phi\Gamma_z}{2\pi\varepsilon}\right], \tag{57}$$

where Γ_z is the eigenfunction of $\mathfrak{M}_z$ given as one of Eqs. (48), (53), or (42) depending on which case k_z^i belongs to, and Φ is the expansion coefficient given as

$$\Phi = \int \Gamma_z^* F dz \Big/ \int |\Gamma_z|^2 dz, \tag{58}$$

where * signifies the complex conjugate. This is the integral expression of the GF that gives the magnetic scalar potential due to MSSW excitation, which conforms to the standard 2D iFT.

In real experiments, the physical quantity that SRFMR-SKEM detects is not the magnetic potential but the magnetization component normal to the film surface m_{iz}. In this technique, laser pulses illuminate the top surface of the film and the optical power penetrates into a finite depth. Thus the reflected light contains information of the exponentially weighted average of m_{iz} over the penetration depth. Taking this into account, the GF in the same representation as measured by SRFMR-SKEM, G^m, is given as

$$G^m(\vec{r}_t) = -\int_{-s/2}^{s/2}\left(i\kappa\frac{\partial G}{\partial y} + \chi\frac{\partial G}{\partial z}\right)e^{(z-s/2)/\delta_p}dz, \tag{59}$$

where δ_p is the optical penetration depth. Plugging Eq. (57) into Eq. (59) yields the following expression:

$$G^m(\vec{r}_t) = \sum_{k_z^i} \mathcal{F}^{-1}_{\vec{k}_t}\left[\frac{\Phi\Gamma_z^m}{2\pi\varepsilon}\right], \tag{60}$$

where Γ_z^m is given as

$$\Gamma_z^m = \int_{-s/2}^{s/2}\left(\kappa k_y\Gamma_z - \chi\frac{d\Gamma_z}{dz}\right)e^{(z-s/2)/\delta_p}dz. \tag{61}$$

The 2D spatial distribution of the dynamic magnetization response captured by SRFMR-SKEM is proportional to the convolution of $G^m(\vec{r}_t)$ and the wave source distribution. We will focus on this quantity, rather than ψ in the following discussion.

Up to this point, the expression of the GF is mathematically rigorous. However, direct numerical calculation of Eq. (60) requires a very large amount of computational time and resources. Thus the following approximations will be employed to reduce the required computation resources without significantly sacrificing the accuracy:

(1) Equation (60) is for an infinitesimally small point source. In practice, the size of the point wave source can be finite, reflecting the lateral resolution of the measurement technique and the finite spatial frequency of the wave source distribution. For this purpose, the delta function is replaced with a Gaussian having a finite standard deviation:

$$\delta(x)\delta(y) \to \phi_\sigma^r(\vec{r}_t). \tag{62}$$

The Fourier transform of the infinitesimally small point source is also replaced as follows:

$$\frac{1}{2\pi} \to \phi_\sigma^i(\vec{k}_t). \tag{63}$$

(2) All k_z^i other than the solution of the eigenequation belonging to case (1), i.e., $iq_{z0}^i = k_{z0}^i$, are ignored in the summation of Eq. (60), since we are interested in the behavior of the GF in areas sufficiently far away from the point source. Since only real q_{z0}^i can give $\varepsilon = 0$, this should have the dominant contribution to the integration.

With these approximations, G^m can be written as

$$G^m(\vec{r}_t) \approx \mathcal{F}^{-1}_{\vec{k}_t}\left[\frac{\Phi_0\Gamma_{z0}^m\phi_\sigma^i(\vec{k}_t)}{\varepsilon_0}\right]. \tag{64}$$

This expression no longer has a summation because we take into account only q_{z0}^i, and ignore all other k_z^i. The terms appearing in the integrand, Φ_0, Γ_{z0}^m, and ε_0, are obtained by plugging $q_z^i = q_{z0}^i(k_y)$ into Eqs. (47), (48) or (53) depending on the range of k_y, (58), (61), and (46), respectively.

It should be noted that the complex conjugate * and the absolute value $|\ldots|$ are no longer necessary in the inner product and normalization integral appearing in Eq. (58) because Γ_z associated with q_{z0}^i is real. This indeed has vital importance for the numerical calculation of Eq. (64). Equation (64) has singularities because ε_0 can take 0 at certain points of $\vec{k}_t$. In order to calculate such an improper integral, we need to perform complex integration using Cauchy's theorem. If the integrand had * and $|\cdots|$, it would be a nonholomorphic function which invalidates Cauchy's theorem. In reality, we take into account only the discrete solutions of the eigenequation k_{zn}^i (in this work, only $k_{z0}^i = iq_{z0}^i$) in Eq. (64). The eigenfunctions associated with the discrete solutions are always real, and therefore * and $|\cdots|$ can be removed in Eq. (58). This guarantees the holomorphicity of Φ_0. Obviously all other terms in the integrand of Eq. (64) are holomorphic functions, though the dependence of q_{z0}^i on k_y is very complicated. This holomorphicity validates Cauchy's theorem and enables one to compute Eq. (64) by complex integration.

The concrete forms of the terms appearing in Eq. (64) are presented here:

$$\Gamma_{z0}^m = e^{-s/2\delta_p}\left[\left(\chi q_{z0}^i - \kappa k_y\right)(1+R_0)\frac{\sinh\left\{\left(1/\delta_p + q_{z0}^i\right)s/2\right\}}{1/\delta_p + q_{z0}^i}\right.$$
$$\left.-\left(\chi q_{z0}^i + \kappa k_y\right)(1-R_0)\frac{\sinh\left\{\left(1/\delta_p - q_{z0}^i\right)s/2\right\}}{1/\delta_p - q_{z0}^i}\right], \tag{65}$$

$$\Phi_0 = \begin{cases} \Phi_{V0} = \frac{2\sinh(q_{z0}^i s/2)}{q_{z0}^i N_0} & F = F_V, \\ \Phi_{S0} = \frac{2R_0\sinh(q_{z0}^i s/2)}{N_0} & F = F_S, \end{cases} \tag{66}$$

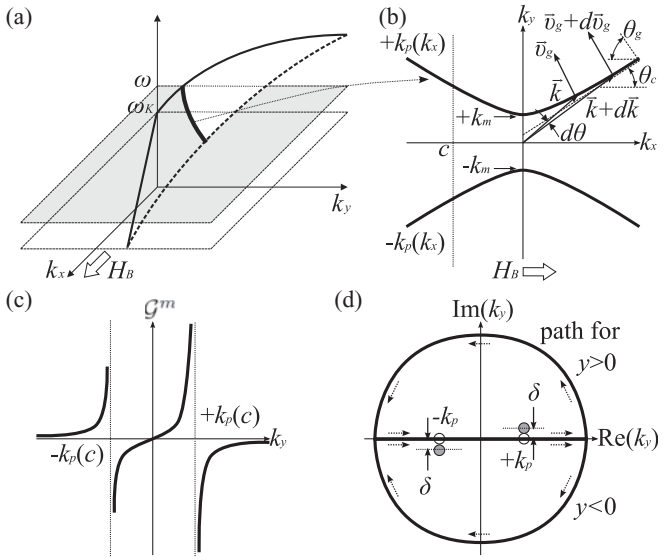

FIG. 3. (a) Dispersion surface of MSSWs originally presented in Ref. 1. ω_K is the uniform (Kittel) mode frequency. This surface is symmetric with respect to both k_x and k_y axes. (b) Slowness surface given as a cross section of the MSSW dispersion surface cut by a constant frequency plane at ω in (a). (c) Profile of $\mathcal{G}^m$ along a line of $k_x = c$ in (b). (d) Integration path for positive/negative y. With the addition of $i\delta$ to k_p, the positive and negative poles move upward and downward, respectively.

$$N_0 = \frac{s}{2}\left[\left(1-R_0^2\right)\left(\frac{1}{q_{z0}^e s}+1\right)\right.$$
$$\left.+\left(1+R_0^2\right)\left\{\frac{\cosh\left(q_{z0}^i s\right)}{q_{z0}^e s}+\frac{\sinh\left(q_{z0}^i s\right)}{q_{z0}^i s}\right\}\right], \quad (67)$$

$$R_0 = \frac{\kappa k_y}{(1+\chi)q_{z0}^i + q_{z0}^e \tanh\left(q_{z0}^i s/2\right)}. \quad (68)$$

F. Algorithm for numerically calculating the Green's function

Figure 3(a) shows the dispersion surface of MSSWs originally derived by the DE theory. This surface is symmetric with respect to both k_x and k_y axes. In SRFMR-SKEM, the excitation frequency is fixed during measurement. The dispersion relation of MSSWs in the k_x-k_y space under a constant ω, called the slowness surface, is given as the cross section of the MSSW dispersion surface cut by a constant frequency plane, as shown in Fig. 3(b).[2] The positive and negative slowness surfaces are denoted as $\pm k_p(k_x)$, respectively.

For explanations given below, the integrand function excluding the Gaussian in Eq. (64) is denoted as

$$\mathcal{G}^m = \frac{\Phi_0 \Gamma_{z0}^m}{\varepsilon_0}. \quad (69)$$

This becomes singular on the slowness surfaces because $\varepsilon_0 = 0$ on them. Figure 3(c) shows the profile of $\mathcal{G}^m$ along the $k_x = c$ line. The positions of these singularities are symmetric with respect to the origin, but their strength, i.e., residue, is different between the negative and positive side, which gives rise to the field displacement nonreciprocity of MSSWs. In order to numerically calculate such an improper integral, the following algorithm is adopted.

In the 2D iFT of Eq. (64), the 1D iFT along the k_y axis must be performed first because performing the iFT along k_x first causes it to diverge at $k_y \to \pm k_m \mp 0$. Prior to performing the iFT along k_y, the integrand is separated into the singular part $\mathcal{G}_s^m$ and the regular part $\mathcal{G}_r^m$ as follows:

$$\mathcal{G}_s^m = \left(\frac{R_p}{k_y - k_p} + \frac{R_n}{k_y + k_p}\right), \quad (70)$$

$$\mathcal{G}_r^m = \mathcal{G}^m - \mathcal{G}_s^m, \quad (71)$$

where R_p and R_n are residues given as

$$R_{p/n} = \lim_{k_y \to \pm k_p} (k_y \mp k_p)\mathcal{G}^m. \quad (72)$$

This is equivalent to separating the GF into the nonpropagating (evanescent) and propagating components.

The 1D iFT of the regular part along k_y, including the Gaussian

$$\mathcal{F}_{k_y}^{-1}\left[\mathcal{G}_r^m \phi_\sigma^i(k_y)\right], \quad (73)$$

can be easily calculated by the standard fast Fourier transform (FFT) routine because the integrand is a well behaved function having no singularity, and the integration range can be reduced from $\pm\infty$ to a finite range ($\approx \pm 2\pi/\sigma$ is usually sufficient) due to the Gaussian in the integrand, which rapidly rolls off as k_y^2 becomes larger.

The 1D iFT of the singular part, which represents the propagating wave component of the GF, along k_y is calculated as follows. If the iFT integration is performed strictly along the real k_y axis, the result contains both incoming and outgoing waves, thus the result becomes the standing-wave solution. In the real experiment, we do not see any incoming waves so we have to take into account only the outgoing wave component. For this purpose, an infinitesimally small imaginary value $i\delta$ is added to k_p in Eq. (70):

$$\mathcal{G}_s^m = \left(\frac{R_p}{k_y - k_p - i\delta} + \frac{R_n}{k_y + k_p + i\delta}\right). \quad (74)$$

Physically, this is equivalent to giving a very small loss to the system under consideration. With this small loss, the positive and negative poles move up and down, respectively, as shown in Fig. 3(d). The 1D iFT of Eq. (74) can be analytically calculated by integrating along the path shown in the figure and applying Jordan's lemma:

$$\mathcal{F}_{k_y}^{-1}\left[\mathcal{G}_s^m\right] = \begin{cases} \sqrt{2\pi}\, i R_p e^{ik_p y} & y > 0 \\ \sqrt{\pi/2}\, i(R_p - R_n) & y = 0 \\ -\sqrt{2\pi}\, i R_n e^{-ik_p y} & y < 0 \end{cases}. \quad (75)$$

Inclusion of the Gaussian can be accomplished by utilizing the convolution theorem. For the FT/iFT defined as Eqs. (1) and (2), the convolution theorem becomes

$$\mathcal{F}_{k_y}^{-1}\left[\mathcal{G}_s^m\right] \otimes \phi_\sigma^r(y) = \sqrt{2\pi}\,\mathcal{F}_{k_y}^{-1}\left[\mathcal{G}_s^m \phi_\sigma^i(k_y)\right], \quad (76)$$

where $\otimes$ signifies convolution. Numerical calculation of this convolution can be easily implemented using Eqs. (75) and (3).

After the iFT along the k_y axis is done, the integrand no longer has any singularities. Thus the iFT along the k_x axis, including the Gaussian

$$G^m(\vec{r}_t) = \mathcal{F}_{k_x}^{-1}\left[\mathcal{F}_{k_y}^{-1}\left[\left(\mathcal{G}_r^m + \mathcal{G}_s^m\right)\phi_\sigma^i(k_y)\right]\phi_\sigma^i(k_x)\right], \quad (77)$$

can again be easily performed using the standard FFT routine.

G. Inclusion of finite damping

The above formalism up to Eq. (73) has been based on the lossless assumption, but an infinitesimally small loss was added in Eq. (74) in order to exclude the incoming wave components. On the other hand, Sturm-Liouville operators require that both $p(z)$ and $q(z)$ should be real.

Under the limit of $\delta \to 0$, the MSW operator $\mathfrak{M}$ still remains Hermitian because it can be shown that $\mathfrak{M}_z$ satisfies the following Hermitianity condition:

$$\langle \Gamma_{zm}|\mathfrak{M}_z|\Gamma_{zn}\rangle = \langle \Gamma_{zn}|\mathfrak{M}_z|\Gamma_{zm}\rangle^*, \quad (78)$$

where $\langle\cdots\rangle$ is Dirac's bra-ket notation.

Now we discuss how to incorporate a finite loss into the magnetic film. The magnetization dynamics with a finite loss are expressed by the Landau-Lifshitz-Gilbert (LLG) equation:

$$\frac{d\vec{M}}{dt} = -\gamma\vec{M}\times\vec{H} + \frac{\alpha}{M}\vec{M}\times\frac{d\vec{M}}{dt}. \quad (79)$$

By using Eq. (79) instead of Eq. (5), Polder's susceptibility tensor for a lossy magnetic system can be obtained:

$$P' = \begin{pmatrix} 0 & 0 & 0 \\ 0 & \chi' & -i\kappa' \\ 0 & i\kappa' & \chi' \end{pmatrix},$$
$$\chi' = \frac{(\omega_H - i\alpha\omega)\omega_M}{(\omega_H - i\alpha\omega)^2 - \omega^2}, \quad (80)$$
$$\kappa' = \frac{\omega\omega_M}{(\omega_H - i\alpha\omega)^2 - \omega^2}.$$

This is equivalent to replacing ω_H with $\omega_H - i\alpha\omega$. A finite value of α makes both $p(z)$ and $q(z)$ of $\mathfrak{M}_z$ complex. Thus $\mathfrak{M}$ is no longer Hermitian under the lossy condition. This invalidates the expression of the GF given as a summation of eigenfunctions as shown in Eq. (57), because the orthogonality of the eigenfunctions is broken. The broken orthogonality gives rise to cross coupling between two different order eigenfunctions, meaning that energy of one mode leaks to other modes. Also, the eigenfunctions for the discrete solutions belonging to either case (1) or (2) are no longer real but take complex values. This necessitates a complex conjugate * and absolute value $|\cdots|$ when calculating the function inner product and normalization integral in Eq. (58), which invalidate holomorphicity of the integrand function.

However, we assume that the approximate expression of the GF, Eq. (64), should be still reasonably accurate as it is even with a finite loss due to the following reasons. First, the cross coupling and the deviation of the expansion coefficient are proportional to α, and therefore expected to be reasonably small for a sufficiently small α. Second, the lowest-order eigenfunction Γ_{z0}^m should have the dominant contribution to the total GF as the lowest-order eigenvalue ε_o is much smaller than other eigenvalues. The appreciable effects expected from a finite α are first a finite propagation decay of MSSWs emitted by a point source, which should be properly expressed by Eq. (64), and second a small deviation of the coupling coefficient from the excitation field to the lowest eigenfunction. Apart from the change of the coupling coefficient, the further $\vec{r}_t$ moves away from the excitation source, the more accurate Eq. (64) should become as the contributions from other eigenfunctions due to energy leakage diminish.

As for the numerical calculation of Eq. (64), the same algorithm as presented in the above subsection can be used, because Eq. (64) is still holomorphic even with a finite α, and it was confirmed that the inclusion of finite α as explained here moves the poles in the same directions as shown in Fig. 3(d), but of course, by a finite distance. The calculation just needs to use complex parameters P', χ', and κ', as given in Eq. (80).

Theoretically, it is possible to numerically calculate the GF by directly applying the standard FFT routine to Eq. (64), because the integrand function $\mathcal{G}^m$ no longer has any singularity on the real k_y axis if the system has a finite loss. That way, it is possible to perform the iFT even if the integrand function is nonholomorphic. However, the discretization step in the numerical integration of the iFT must be sufficiently smaller than the distance of the pole from the k_y axis in order to achieve a good accuracy. This may actually require larger computational resources than the algorithm presented in this work, especially for small α. This requirement is equivalent to saying that a sufficiently large area in real space has to be included in the numerical calculation such that MSSWs emitted from the point source at the origin completely damp out before reaching the edges of the area and no reflection occurs.

H. General characteristics of the Green's functions of MSSWs

Figure 4 shows the GFs of MSSWs in the same representation as measured by SRFMR-SKEM for both fictitious volume charges G_V^m and surface charges G_S^m calculated by our approach. This calculation was performed with the following parameters: $H_B = 3.42\times10^4$ A/m, $f = 8$ GHz, $M_s = 7.96\times10^5$ A/m, $\gamma = 2.39\times10^5$ rad m/s A (corresponding to $g = 2.16$) and α is set to either 0 or 0.0074 for a lossless or lossy magnetic film, respectively. These parameters are the same as in the experiments presented later in this paper except for H_B. The GFs are symmetric with respect to the y axis but slightly asymmetric with respect to the x axis due to the field displacement nonreciprocity.[28] Thus only the right half is shown for each image.

These images clearly show strong anisotropy of the GF of MSSWs, reflecting the polar nature of the spin system. The amplitude images show that the MSSW propagation from the point source is confined within a certain angular range with respect to the y axis. Also seen is a significant increase of the MSSW amplitude along the limit angles of the angular range of wave propagation. The phase distribution is totally different from that of standard 2D isotropic waves. The wave front is not concentric but more or less parallel to the x axis both inside and outside the angular range of wave propagation, and becomes quite complicated along the limit angles.

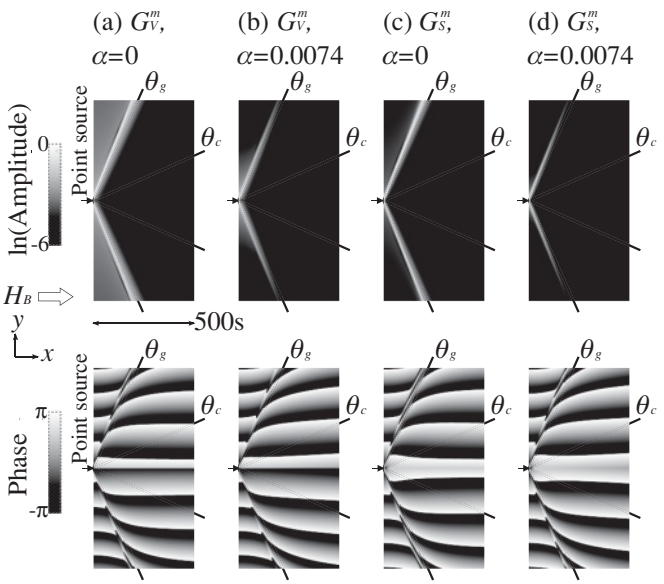

FIG. 4. GFs of MSSWs, represented as the polar Kerr signal, which is measured by SRFMR-SKEM. In the amplitude images, the brightness is assigned proportional to the natural log of the normalized amplitude in the range of (−6,0). In the phase images, brightness stands for the phase. White and black correspond to π and $-\pi$, respectively. The four lines in each image show θ_c and θ_g, respectively. Only the right half of each image is shown because these are symmetric with respect to the y axis, but slightly asymmetric with respect to the x axis due to the field displacement nonreciprocity.

The limit angle of the energy flow from the point source due to MSSW propagation is given by the following argument.[13,24] As shown in Fig. 3(b), the slowness surface of the MSSW asymptotically approaches straight lines as $|\vec{k}_t|$ becomes larger, so the angle of $\vec{k}_t$ is limited between these asymptotes. This limit angle is defined as the critical angle for the wave vector θ_c, given as

$$\theta_c(\omega) = \sin^{-1}\left(\frac{\sqrt{\omega^2 - \omega_K^2} + \omega}{\omega_H + \omega_M}\right). \tag{81}$$

In the limit of $\omega \to \omega_K$, this expression becomes particularly simple as $\theta_c = \tan^{-1}(\sqrt{H_B/M_S})$[1]. The vectorial expression of the group velocity is given as $\vec{v}_g = \nabla_k \omega$. This indicates that the direction of energy flow set by $\vec{v}_g$ is perpendicular to the tangent of the slowness surface, as shown in Fig. 3(b). Thus the angle of energy flow is limited between $\pi/2 \pm \theta_c$ with respect to the y axis, which is defined as the critical angle for the group velocity θ_g. θ_c and θ_g are calculated as 23.9° and 66.1°, respectively, using Eq. (81) and the parameters given above. The angular range of MSSW propagation shown in the images in Fig. 4 agrees very well with the calculated value of θ_g.

The amplitude increase seen in these images is a "semicaustic" beam due to focusing of MSSWs. In general, caustic beams are formed where the curvature of the slowness surface vanishes, i.e., $d^2k_y/dk_x^2 = 0$. The point that satisfies this condition will be referred to as a caustic point. The MSSW slowness surface does not have a caustic point, thus does not form a "real" caustic beam. But the curvature asymptotically decreases down to zero as the angle of $\vec{k}_t$ approaches θ_c, causing semicaustic beams of the MSSW along the θ_g directions.[2]

MSBVWs also form caustic beams.[13] It is interesting, and actually important, to see the amplitude behaviors of the caustic beams of both the MSSW and MSBVW when performing the GF calculation on these modes.

Let us first discuss the behavior of the semicaustic beams of the MSSW. Figure 3(b) shows that waves carrying energy in the direction between $\vec{v}_g$ and $\vec{v}_g + d\vec{v}_g$ actually have a wave vector between $\vec{k}_t$ and $\vec{k}_t + d\vec{k}_t$. If we define the mode density as a function of angle of $\vec{k}_t$ as $g(\theta) = |d\vec{k}_t/d\theta|$, $g(\theta)$ increases as θ approaches θ_c, and diverges at θ_c. On the other hand, it can be shown that the coupling between a plane MSSW and a point source remains finite for any angle of $\vec{k}_t$. Thus the amplitude of the semicaustic beam should diverge if the point source were infinitesimally small. In the calculation, the point source is assumed to be of finite size, Gaussian with standard deviation $\sigma = 2.5s$ to guarantee fast convergence. This causes waves having a too large wave number to be filtered out. Consequently, the magnitude of the integrand exponentially decreases as the angle of $\vec{k}_t$ approaches θ_c, outweighing the divergence of the mode density, and eventually the amplitude of the caustic beam is suppressed to a finite value.

Next we consider the behavior of the caustic beams of the MSBVW. The MSBVW slowness surface has maximum of two caustic points for each quadrant depending on the condition. Also, it can be shown that the slowness surface asymptotically approaches straight lines whose slope is $\pm 1/\sqrt{-(1+\chi)}$ as $|\vec{k}_t|$ becomes large (note that MSVBWs are excited when $1 + \chi < 0$, thus the slope given here is real). This means that it forms zero, four, or eight real caustic beams and four semicaustic beams in total.[2]

The caustic points on the MSBVW slowness surface occur at a finite $\vec{k}_t$ if they exist. It can be shown that the amplitude of the caustic beam is inversely proportional to the third derivative of the slowness surface, which is in general finite.[13] Therefore the amplitudes of these real caustic beams of the MSBVW stay finite. On the other hand, the amplitudes of the semicaustic beams should diverge for the same reason as for MSSWs if an infinitesimally small point wave source emits MSBVWs.

These arguments are based on pure dipole interaction. In reality, if $|\vec{k}_t|$ becomes large, exchange interaction bends the slowness surface. For this reason, the amplitude of the semicaustic beam can never diverge even if the point source is infinitesimally small.

Figure 4 also shows the GFs for a lossy magnetic film. The effect of a finite damping is seen as an exponential decay of the MSSW amplitude (linear slope in the log plot) as they propagate away from the point source. However, the damping does not seem to have any appreciable effect on the phase distribution. This is consistent with the experimental result that the decay constant of the MSSW propagating along the y axis (imaginary part of the complex k_m) is very sensitive to the Gilbert damping factor α, while the wave number (real part of the complex k_m) is not.[21]

I. Differences between the two Green's functions of MSSWs

The theory presented in this work derived two GF of MSSWs, one for fictitious volume charges G^m_V and the other

for surface charges G_S^m. Thus some comments about the differences between these two GFs are in order.

These GFs share the same general characteristics discussed in the previous subsection, such as limited propagation angle and formation of semicaustic beams. The major difference is seen in the phase distribution. The GFs for fictitious volume charges G_V^m and surface charges G_S^m have nearly antisymmetric and symmetric phase distribution with respect to the x axis, respectively. A fictitious volume charge source, shown in the RHS of Eq. (26), located at the origin, generates static magnetic fields radially in the outward directions. These fields exert torque on magnetic moments in the outward direction with respect to the x axis, meaning that magnetic moments in the positive y region are tipped out to the positive y direction, and vice versa. As a result, the phase distribution shows an abrupt 180° change, and the amplitude of G_V^m becomes zero near the x axis. The reason why this transition is not right on the x axis is due to the field displacement nonreciprocity of MSSWs, which causes a finite offset between the amplitudes of the MSSWs propagating in the positive and negative y directions. On the other hand, the GF for surface charges, G_S^m, does not show such an abrupt phase jump or zero amplitude near the x axis. The surface charge source, shown in the RHS of Eq. (27), has two delta functions at the top and bottom surfaces of the film ($z = \pm s/2$). This means that the same magnitude of positive and negative charges are induced at these boundaries, which act as a dipole oriented along the z axis. The magnetic fields generated by a dipole located at the origin exert torque in the same direction along the z axis to magnetic moments both in positive and negative y region, which results in smoothly varying amplitude and phase distributions for G_S^m. The reason why G_S^m is not completely symmetric with respect to the x axis is again due to the field displacement nonreciprocity of MSSWs.

Another difference to be pointed out is that under the condition commonly met in parametric pumping measurements, G_V^m is generally much smaller than G_S^m. In parametric pumping, a metal layer is deposited on top of the magnetic film with some kind of insulation layer in between to electrically separate them. This metal layer is patterned to form an antenna and excitation currents flow through it to excite MSWs. Thus j_e lies in the x-y plane. The total $\vec{h}_e$ is given by integrating magnetic fields generated by current elements according to Biot-Savart's law as expressed by the first term of Eq. (12).

Magnetic fields generated by the x component of the ac current density do not have a x component and thus do not contribute to the induction of fictitious volume charges. On the other hand, magnetic fields from the y current component have a x component thus contribute to the induction of the fictitious volume charges, but do not have a y component. Therefore the strength of the fictitious volume charge source, shown as the first term in the RHS of Eq. (25), can be written by using Eq. (20) as

$$\chi \frac{\partial h_{\mathrm{ex}}}{\partial x} = -\chi \frac{\partial h_{ez,y}}{\partial z}, \tag{82}$$

where $\vec{h}_{e,y}$ is the excitation field from the y current component, not the total excitation field distribution. This equation means that the strength of the fictitious volume charge source is proportional to the field gradient along the z axis of the magnetic field coming from the y component of the ac current density.

Let us turn to the strength of the surface charge source shown as the second term in the RHS of Eq. (25). This is expanded as

$$P\vec{h}_e \cdot \vec{e}_z = i\kappa h_{ey} + \chi h_{ez}. \tag{83}$$

This equation shows that the strength of the surface charge source is proportional to the field strength itself, and the proportionality constant is of the same order of magnitude as for the fictitious volume charge source.

In the beginning of the theory, it was assumed that the excitation field sources are sufficiently far away from the magnetic film such that the field distribution can be approximated as uniform across the film thickness. This can be mathematically expressed as $\partial h_{ei}/\partial z \cdot s \ll h_{ei}$ $(i = x,y,z)$. This condition dictates that the fictitious volume charge sources are much smaller than the surface charge sources except for some limited points where the surface charge source vanishes.

If the metal layer is directly deposited on a magnetic film, which is possible for magnetic insulators such as YIG, the field gradient in the interior of the film can be sufficiently large that the fictitious volume charge sources become comparable to the surface charge sources. In this case, however, the above assumption is of course no longer valid, thus the problem becomes 3D, which significantly complicates the theory and requires much more computation resources.

III. APPLICATION OF THE GREEN'S FUNCTION TO RECONSTRUCTION OF THE SPATIAL MSSW PROPAGATION PATTERNS

A. Experimental setup

We experimentally observed the spatial MSSW propagation patterns using SRFMR-SKEM under three different cases, one for 1D propagation along the direction perpendicular to the bias field, and the other two for 2D diffraction patterns around different irregularities. The experimental details are presented in this subsection.

The details of SRFMR-SKEM apparatus have been presented elsewhere.[20–22] We used two samples for these three measurements. The configurations of the two samples are shown in Fig. 5. These are 100-nm-thick Py coupons patterned into a square size of 1×1 mm^2. Magnetic properties are as given in the calculation of the GFs. A coplanar waveguide (CPW) with a total width of 18 μm and a center conductor width of 3 μm is formed along the horizontal center line by patterning a 750-nm-thick Cu layer separated from the Py layer with a 540-nm-thick alumina layer. During measurement, a dc bias field H_B is applied along the CPW, and a continuous sinusoidal current at a frequency f between 2 and 8 GHz is fed to one side of the CPW. f and H_B are set to satisfy $\omega > \omega_K$ in order to selectively excite MSSWs. The SRFMR-SKEM measures the polar Kerr rotation from the top surface of the Py layer with an optical penetration depth δ_p estimated as 15 nm.

Experiment 1 is the measurement of the 1D profile of the dynamic magnetization along the y axis, which was already

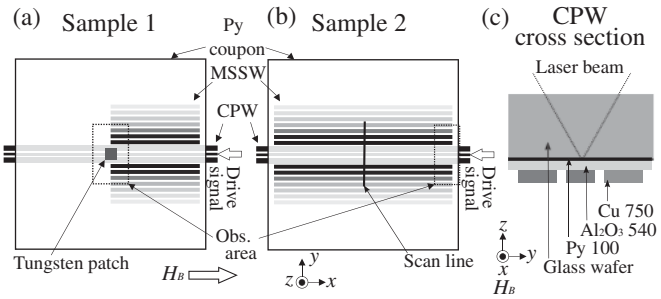

FIG. 5. (a) and (b) Top view of the two samples. (c) Cross section of the layer structure of these samples. They consist of a 100-nm-thick Py coupon with a size of 1×1 mm^2 and a coplanar waveguide (CPW) with a total width of 18 μm and center conductor width of 3 μm running along the horizontal center line. The CPW was formed by patterning a 750-nm-thick Cu layer on top of a 540-nm-thick alumina layer. Sample 1 has a W patch at the center that shorts the CPW. Sample 2 has the same structure, except for no W patch. During measurement, a dc bias field is applied parallel to the CPW. In experiment 1, the dynamic magnetization is measured along the line perpendicular to the bias field on sample 2 while a sinusoidal excitation current at $f = 8$ GHz is sent to the CPW. The line in (b) clarifies the scanning orientation for this measurement. In experiments 2 and 3, a sinusoidal excitation current at 2–8 GHz is fed to the CPW, and the dynamic magnetization is acquired in the rectangular area shown in samples 1 and 2, respectively. Also given in this figure are coordinate definitions.

published in Ref. 21. An excitation current at $f = 8$ GHz is sent to the CPW, and SRFMR-SKEM measures the amplitude and phase of the dynamic magnetization along the centerline of the Py coupon perpendicular to the CPW in sample 2. The line in Fig. 5(b) clarifies the scanning orientation.

Experiments 2 and 3 are measurements of 2D diffraction patterns of MSSWs created around different irregularities, each of which were captured in samples 1 and 2, respectively. For experiment 2, a tungsten (W) patch is deposited at the center of sample 1 to shorten the CPW, so the excitation current flows to the center and is reflected back at the W patch. Thus MSSWs are excited along only the right half of the CPW. The dynamic magnetization is captured in the rectangular area around the W patch, shown in Fig. 5(a). In experiment 3, sample 2 has the same CPW but without the W patch so that the excitation current flows all the way through the CPW. The dynamic magnetization is captured in the rectangular area near the vertical edge shown in Fig. 5(b).

B. Experiment 1: Measurement and analysis of 1D spatial distribution of propagating MSSWs

For the study of MSSWs, a 1D system invariant along the bias field (x axis) is often of particular interest because MSSWs predominantly propagate along the direction perpendicular to the bias field (y axis). For this reason, we first applied the GF obtained in this work to the analysis of experiment 1, which excites MSSWs propagating along the y axis. Since the characteristic decay length is much shorter than the lateral size of the Py coupon, MSSWs excited by the CPW along the horizontal centerline propagate in both positive and negative y directions, and completely damp out before reaching the edges

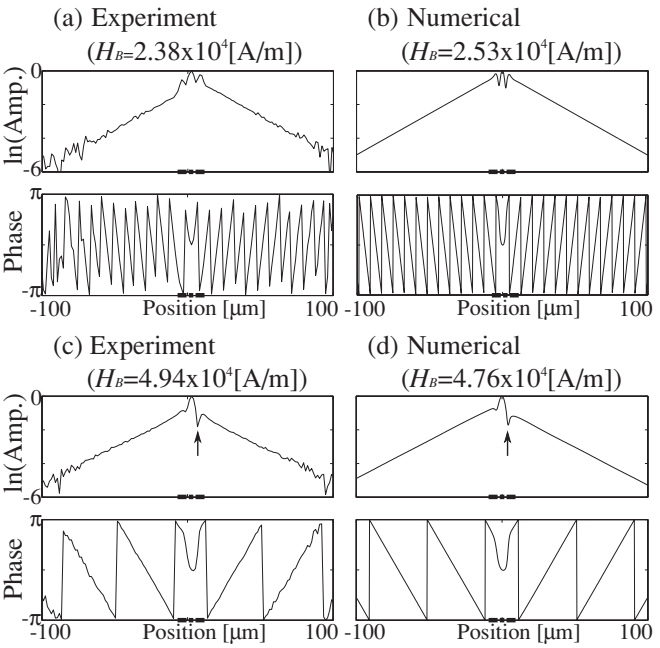

FIG. 6. Comparison of the experimentally observed and numerically calculated 1D spatial distribution of the dynamic magnetization on a 1 mm $\times$ 1 mm Py coupon without a W patch (sample 2 in Fig. 5) scanned along a line perpendicular to the bias field. Excitation frequency is 8 GHz, and the bias field is 2.38×10^4 (A/m) for (a) and 4.94×10^4 (A/m) for (c), respectively. The bias field in the numerical calculation is fitted to 2.53×10^4 (A/m) for (b) and 4.76×10^4 (A/m) for (d) in order to match the wave number to the experimental result. Three segments of bold lines at the bottom of each figure show the position of the CPW. The arrow shown in the amplitude plot of (c) and (d) indicates the cusp mentioned in the text.

of the coupon. Thus this measurement observes the decaying plane MSSWs.

It is clear that sample 1 does not have any x component of the excitation field, so the fictitious volume charge is not present as mentioned above. Also, convolving the 2D GF with a wave source distribution invariant along the x axis is equivalent to simply taking the dc component along the x axis. Thus the 1D GF can be obtained by setting $k_x = 0$ and performing the iFT on G_S^m along the k_y axis, i.e.,

$$G^m_{\mathrm{MSSW}}(y) \approx \mathcal{F}^{-1}_{k_y}\left[\frac{\Phi_{S0}\Gamma^m_{z0}\phi^i_\sigma(k_y)}{\varepsilon_0}\right]\Bigg|_{k_x=0}. \tag{84}$$

This 1D GF is convolved with the wave source distribution calculated from the CPW geometry. The comparison between the experimentally observed and numerically calculated 1D spatial distribution of the dynamic magnetization under two different H_B values is shown in Fig. 6. The value of H_B used in the numerical calculation is fitted to match the wave number to the experimentally observed value and thus is slightly different from H_B used in the experiment. They show in general very good agreement. The shape of the plot is very similar between the experimental and numerical results for both bias fields. Only a slight disagreement is observed around the CPW in the amplitude profile for the lower bias field (shorter wavelength), i.e., (a) and (b). This is

considered to be due to inaccurate current distribution used in the numerical calculation, which assumes a plane current sheet evenly spreading out the entire CPW conductor. The real current distribution may be somewhat different from this assumption due to current crowding effect, capacitive coupling between the CPW and the Py coupon, and so on, which alter the wave source distribution, and consequently the amplitude profile of the dynamic magnetization around the CPW. For the higher bias field (longer wavelength), the agreement is excellent for both the amplitude and phase plot as shown in (c) and (d).

One peculiar feature revealed by this analysis is the sharp cusp in the amplitude plot, which is pointed by an arrow in (c) and (d). This appears only on one side of the two gaps of the CPW, and this becomes more prominent as the wavelength becomes "longer". This behavior is opposite to the well known field displacement nonreciprocity of the MSSW, which becomes more prominent as the wavelength becomes "shorter."

The cause of this cusp is interpreted as follows. The source distribution is obtained by first calculating the excitation field using the first term of Eq. (12), then calculating Eq. (83). According to Eq. (83), the real and imaginary part is coming from the z and y components of the excitation field, respectively, thus these are phase shifted by 90° to each other. Consequently, the excitation field is not linearly but elliptically polarized. Because the CPW geometry is symmetric, so is the excitation field distribution with respect to the x axis. This means that the "helicity" of the elliptically polarized excitation field is opposite between the negative and positive y region. The LL equation, (5), says that the magnetic moment precesses in only one helicity direction (clockwise direction). Thus the coupling between the excitation field and the spin precession is different between the negative and positive y region, and becomes minimum if the helicity of the excitation field is counterclockwise, and its ellipticity coincides with the inverse of the ellipticity of the magnetization precession. In reality, MSSWs propagate in both directions so wave interference also comes into play to complicate the profile even further.

It is not easy to come up with an intuitive interpretation of this cusp observed in both experimental and numerical results without having the correct mathematical description of the surface charge source term. The successful reproduction of this cusp in the numerical calculation is considered one piece of powerful evidence that proves the correctness of the theory derived in this work.

C. Experiment 2: Measurement and analysis of 2D diffraction pattern of MSSWs around the W patch

We carried out the measurements of 2D spatial distributions of MSSWs around the W patch in experiment 2. As the first step of the experiments, the spatial distribution of dynamic magnetization was captured with varying the frequency and amplitude of the excitation current, and the bias field. These results showed first that the amplitude is proportional to the excitation current, and second that the spatial distribution patterns are solely determined by the wavelength of the MSSWs and are independent of frequency.[22] These observations indicate the linearity of the system and the absence of exchange fields

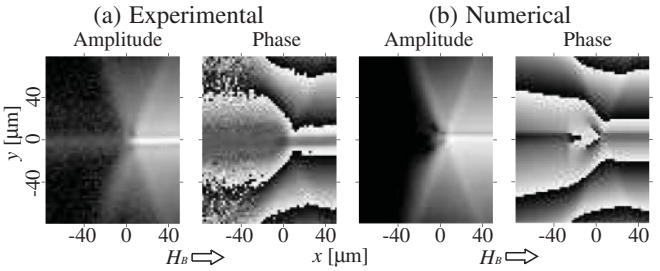

FIG. 7. Comparison of the experimentally observed and numerically calculated diffraction patterns in experiment 2. The same brightness scales as in Fig. 4 are used for both amplitude and phase images. The W patch is located at $(x,y) = (0,0)$ in the figure. The experimental result was taken with $H_B = 5.07 \times 10^4$ A/m and $f = 8$ GHz, and showed the wavelength along the y axis as 53.7 μm. In the numerical calculation, H_B was set to 4.73×10^4 A/m in order to match the wavelength.

thus suggesting that the observed spatial distributions are diffraction patterns of pure MSSWs.

In order to verify this interpretation, the spatial diffraction patterns for these measurements were calculated by convolving the GF for a lossy system derived in this work and the wave source distribution in sample 1 using Eqs. (12) and (28). The comparison between experimentally observed and numerically calculated results is shown in Fig. 7. The experiment was done with $H_B = 5.07 \times 10^4$ A/m and $f = 8$ GHz, and showed the wavelength along the y axis as 53.7 μm. In the numerical calculation, H_B was fitted to 4.73×10^4 A/m in order to match the wavelength. Both the amplitude and phase distributions showed excellent agreement. In the amplitude distribution, the decay of the MSSWs along the y axis agrees almost perfectly, and an amplitude increase extending from the W patch along the θ_g direction seen in the experimental result is successfully reproduced in the numerical result, which reflects the semicaustic beams due to focusing of MSSWs, shown in Fig. 4(a).

D. Experiment 3: Measurement and analysis of 2D diffraction pattern of MSSWs near the edge perpendicular to the bias field

In order to calculate the diffraction patterns observed in experiment 3, the boundary condition of the vertical edge must be known. To the author's knowledge, however, there has been no past work that treated the behavior of MSWs reflected by an edge perpendicular to the bias field. This is because the static field distribution and the static domain structure are highly inhomogeneous due to demagnetization fields coming from the edge and an edge domain formed as a result of it. In this work, a simple assumption was made that the vertical edge acts as a strongly pinned boundary for MSSWs having a sufficiently longer wavelength than the inhomogeneous region. Under this assumption, the spatial distribution can be calculated by assuming a mirror image of the wave source distribution and integrating all waves coming from both the real and mirror image wave source distributions.

The experimental and calculation results of experiment 3 are shown in Fig. 8. The parameters, such as H_B and f, are the same as for experiment 2. Again, the agreement is excellent

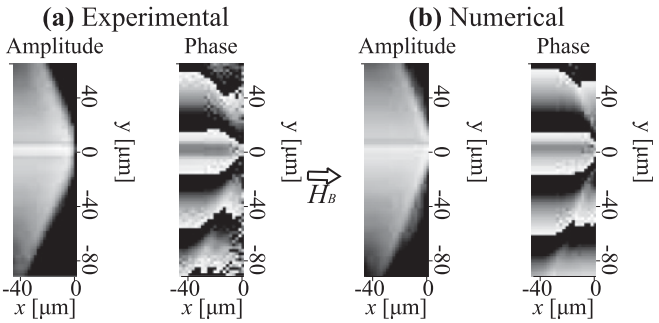

FIG. 8. Comparison of the experimentally observed and numerically calculated diffraction patterns in experiment 3. The same brightness scales as in Fig. 4 are used for both amplitude and phase images. The CPW enters beneath the sample at $(x,y) = (0,0)$ in the figure. The parameters, such as H_B and f, are the same as for experiment 2.

for both amplitude and phase. The numerical calculation reproduced all major features of the experimentally observed MSSW distribution, including the decay of MSSWs along the y axis, amplitude increase along the θ_g direction, and the shape of the phase distribution.

IV. CONCLUSION

We developed the 2D GF of MSSWs in real space and the frequency domain, $\vec{m}(\vec{r},\omega)$, and used it to calculate the 1D spatial propagation profiles and 2D diffraction patterns of MSSWs. These numerical results showed excellent agreement with the experimental results obtained by SRFMR-SKEM over wide range of bias fields (equivalently wavelength) and successfully reproduced all major features characteristic of MSSWs, such as the strongly anisotropic propagation and caustic beams along θ_g. In experiment 1, the agreement is better for longer wavelengths, probably due to some deviation of the excitation current distribution assumed in the calculation from the real distribution. Regarding experiments 2 and 3, only one comparison between the experimental and numerical results is presented for each experiment in this paper. However, this comparison was made at other bias fields, and they all showed as excellent agreement as in Figs. 7 and 8. These results strongly support the correctness of our approach for deriving the GF presented in this work, and prove the usefulness of the combination of the theoretical and experimental techniques used in this work, i.e., the GF and SRFMR-SKEM, for studying the spatial nature of MSWs.

ACKNOWLEDGMENTS

We would like to thank R. J. M. Veerdonk, T. M. Crawford, and M. Covington for helpful discussions and supplying samples, C. Bowman for W patch deposition, and En Shi for contribution to coding of the numerical calculation script.

*stamaru@andrew.cmu.edu
†www.ece.cmu.edu/ricketts

[1] R. W. Damon and J. R. Eshbach, J. Phys. Chem. Solids **19**, 308 (1961).
[2] V. Veerakumar and R. E. Camley, Phys. Rev. B **74**, 214401 (2006).
[3] F. A. Pizzarello, J. H. Collins, and L. E. Coerver, J. Appl. Phys. **41**, 1016 (1970).
[4] A. B. Valyavsky *et al.*, Sov. Tech. Phys. Lett. **34**, 616 (1989).
[5] N. P. Vlannes, J. Appl. Phys. **62**, 972 (1987).
[6] C. E. Patton, Phys. Rep. **103**, 251 (1984).
[7] S. O. Demokritov, B. Hillebrands, and A. N. Slavin, Phys. Rep. **348**, 441 (2001).
[8] B. A. Kalinikos and A. N. Slavin, J. Phys. C: Solid State Phys. **19**, 7013 (1986).
[9] B. A. Kalinikos and A. N. Slavin, Acta Phys. Pol. A **75**, 541 (1989).
[10] M. G. Cottam, J. Phys. C **12**, 1709 (1979).
[11] R. E. Camley, T. S. Rahman, and D. L. Mills, Phys. Rev. B **23**, 1226 (1981).
[12] O. Buttner, M. Bauer, S. O. Demokritov, B. Hillebrands, Y. S. Kivshar, V. Grimalsky, Y. Rapoport, and A. N. Slavin, Phys. Rev. B **61**, 11576 (2000).
[13] T. Schneider, A. A. Serga, A. V. Chumak, C. W. Sandweg, S. Trudel, S. Wolff, M. P. Kostylev, V. S. Tiberkevich, A. N. Slavin, and B. Hillebrands, Phys. Rev. Lett. **104**, 197203 (2010).
[14] K. Perzlmaier, M. Buess, C. H. Back, V. E. Demidov, B. Hillebrands, and S. O. Demokritov, Phys. Rev. Lett. **94**, 057202 (2005).
[15] K. Perzlmaier, G. Woltersdorf, and C. H. Back, Phys. Rev. B **77**, 054425 (2008).
[16] A. A. Serga *et al.*, Appl. Phys. Lett. **89**, 063506 (2006).
[17] V. E. Demidov *et al.*, Phys. Rev. B **77**, 064406 (2008).
[18] V. E. Demidov, S. Urazhdin, and S. O. Demokritov, Appl. Phys. Lett. **95**, 262509 (2009).
[19] V. E. Demidov *et al.*, Phys. Rev. B **80**, 014429 (2009).
[20] S. Tamaru *et al.*, J. Appl. Phys. **91**, 8034 (2002).
[21] S. Tamaru, J. A. Bain, R. J. M. van de Veerdonk, T. M. Crawford, M. Covington, and M. H. Kryder, Phys. Rev. B **70**, 104416 (2004).
[22] S. Tamaru, Ph.D. thesis, Carnegie Mellon University, Pittsburgh, 2005.
[23] I. Neudecker, M. Klaui, K. Perzlmaier, D. Backes, L. J. Heyderman, C. A. F. Vaz, J. A. C. Bland, U. Rudiger, and C. H. Back, Phys. Rev. Lett. **96**, 057207 (2006).
[24] H. S. Tuan and J. P. Parekh, *RADC Proceedings of the RADC Microwave Magnetics Technolnology Workshop* (1983), p. 207.
[25] L. B. Gol'dberg, Sov. Phys. Tech. Phys. **31**, 1132 (1986).
[26] S. V. Vlaskin and G. M. Novikov, Russian Phys. J. **32**, 262 (1989).
[27] S. Chikazumi, *Physics of Ferromagnetism* (Oxford University Press, Oxford, 1997).
[28] D. D. Stancil, *Theory of Magnetostatic Waves* (Springer-Verlag, New York, 1993).